Selective area molecular beam epitaxy of InSb on InP(111)_B: from thin films to quantum nanostructures

Wijden Khelifi, Pierre Capiod, Clément Barbot, Christophe Coinon, Yves Deblock, N Chaize, M Berthe, P-H Jouneau, S Amarie, Jean-Francois Lampin, et al.

Selective area molecular beam epitaxy of InSb on InP(111)$_B$: from thin films to quantum nanostructures

W.Khelifi[1], P.Capiod[1], C.Barbot[1], C.Coinon[1], Y.Deblock[1], C. N. Santos[1,4], N.Chaize[2], M.Berthe[1], P.-H.Jouneau[3], S.Amarie[5], J.-F.Lampin[1], X.Wallart[1], Ph. Ballet[2], B.Grandidier[1] and L.Desplanque[1]*

[1] *Univ. Lille, CNRS, Centrale Lille, ISEN, Univ. Valenciennes, UMR 8520 - IEMN, F-59000 Lille, France*

[2] *CEA, LETI, Univ. Grenoble Alpes, 38000 Grenoble, France*

[3] *Univ. Grenoble Alpes, CEA, INAC-MEM, 38000 Grenoble, France*

[4] *Univ. catholique de Louvain (UCLouvain), MOST/IMCN, 1348 Louvain-la-Neuve, Belgium*

[5] *Attocube systems AG, Eglfinger Weg 2, 85540 Haar, Germany*

InSb is a material of choice for infrared as well as spintronic devices but its integration on large lattice mismatched semi-insulating III-V substrates has so far altered its exceptional properties. Here, we investigate the direct growth of InSb on InP(111)$_B$ substrates with molecular beam epitaxy. Despite the lack of a thick metamorphic buffer layer for accommodation, we show that quasi-continuous thin films can be grown using a very high Sb/In flux ratio. The quality of the films is further studied with Hall measurements on large-scale devices to assess the impact of the InSb surface and InSb/InP interface on the electronic properties. Taking advantage of the optimized growth conditions for the formation of thin films, the selective area molecular beam epitaxial growth of nanostructures is subsequently investigated. Based on cross-sectional transmission electron microscopy and scanning near-field optical microscopy in the middle-wave infrared, ultra-thin and very long in-plane InSb nanowires as well as more complex nanostructures such as nano-rings and crosses are achieved with a good structural quality.

I. INTRODUCTION

With its low electron effective mass, strong spin-orbit interaction and direct bandgap in the middle-wave infrared spectrum, InSb is very attractive for advanced quantum electronic or optoelectronic nano-devices [1-3]. These applications require a very good crystal quality, which depends on the method of elaboration. Another requirement for quantum applications is the possibility to control precisely the position and shape of the material at the nanoscale to build complex arrays of nanowires, crosses or nano-rings where quantum interference phenomena can occur. Due to the lattice mismatch with other III-V semiconductors, InSb thin film epitaxy on standard III-V substrates (GaAs or InP) implies the growth of a thick accommodation layer to limit the negative impact of threading dislocations on the device performances [4]. Another option is to integrate InSb on a nearly lattice matched CdTe substrate [5-7]. But inter-diffusion of chemical species and fixed charges at the heterovalent interface can seriously degrade electronic or optical material properties. A third approach relies on the bottom-up growth of nanowires (NW) by the metal droplet assisted Vapor Liquid Solid (VLS) growth mode [8-12]. However, the subsequent NW transfer on a host substrate for device processing limits device scalability as well as complex NW network fabrication. In this context, in-plane selective area growth of InSb NW has been demonstrated as a valuable trade-off between the reduction of the area of the incoherent interface between InSb and the mismatched substrate and a well mastered positioning of in-plane nanostructures for their subsequent processing [13] [14]. On a GaAs (100) substrate, the size of InSb islands is limited by the lattice mismatched with the substrate. Achieving several µm long nanowires implies a preliminary reduction of the mismatch using an AlGaSb buffer layer prior to the selective area mask fabrication [13]. On an InP (111) substrate, high quality InSb nanostructures have been demonstrated both by Metal Organic Vapor Phase Epitaxy (MOVPE) under a large partial pressure of trimethyl antimony [14] or by Molecular Beam Epitaxy (MBE) using metal sown epitaxy [15].

In this paper, we show that a very large Sb/In flux ratio during MBE promotes a two dimensional growth mode for InSb on InP(111)$_B$ substrate in strong contrast with the InP (001) substrate. These conditions are subsequently combined with atomic hydrogen selective area growth (SAG) to achieve in-plane InSb nanostructures. Their multi-physical characterization show a high material quality whatever the geometries are.

II. EXPERIMENTAL DETAILS

A RIBER Compact 21 MBE system equipped with valve cracker cells for As and Sb evaporation is used for the growth. As_4 flux is delivered with the cracking zone of the As cell heated at 600°C while Sb flux, mainly composed of Sb dimers, is produced with the cracking zone of the Sb cell heated at 900°C. The system is also equipped with a standard Indium effusion cell and a RF plasma cell that can produce an atomic hydrogen flux. This flux is used for the deoxidization of the substrates but also during all the growth presented in the following. Indium flux is calibrated by recording the RHEED specular intensity oscillation during the homoepitaxy of an InAs layer while As and Sb fluxes are calibrated using V-element limited RHEED specular intensity oscillations during the homoepitaxy of GaAs and GaSb respectively. The growth

chamber is connected under ultra-high vacuum to an X-ray and UV Photoelectron Spectroscopy (XPS-UPS) system.

The growth conditions used for the different samples are summarized in table 1. Five InP (001) substrates are used for the first set of samples. They are deoxidized under As_4 flux and exposed to the atomic hydrogen flux for 30s at 300°C before heated up to 470°C and cooled down before starting the growth. On the first three samples, an InSb layer with a nominal thickness of 10nm is grown at 390°C under a Sb flux of 2ML/s and a nominal growth rate of 0.2 (sample A), 0.1 (sample B) and 0.05ML/s (sample C). For samples D and E, the same nominal thickness is deposited with a growth rate of 0.05ML/s combined with a large Sb flux of 6ML/s at temperatures of 390°C and 405°C respectively.

Table 1- Summary of the parameters used for the growth of the different samples

Sample	Substrate	T_{growth} (°C)	Growth rate (ML/s)	Sb flux (ML/s)	Sb/In flux ratio	Nominal thickness (nm)
A	InP(100)	390	0.2	2	10	10
B	InP(100)	390	0.1	2	20	10
C	InP(100)	390	0.05	2	40	10
D	InP(100)	390	0.05	6	120	10
E	InP(100)	405	0.05	6	120	10
F	$InP(111)_B$	390	0.05	6	120	10
G	$InP(111)_B$	390	0.05	6	120	30
H	$InP(111)_B$	390	0.05	6	120	100
I	Patterned $InP(111)_B$	390	0.2	2	10	10
J	Patterned $InP(111)_B$	390	0.1	2	20	10
K	Patterned $InP(111)_B$	390	0.05	2	40	10
L	Patterned $InP(111)_B$	390	0.05	6	120	10
M	Patterned $InP(111)_B$	390	0.05	6	120	30

The second set of growth is performed on Fe-doped $InP(111)_B$ substrates using the same deoxidization process. InSb is deposited at 390°C under an Sb flux of 6ML/s, an indium flux of 0.05ML/s and with a nominal thickness of 10 (sample F), 30 (sample G) or 100nm (sample H).

For SAG samples, a 30nm thick SiO_2 layer is first deposited on an $InP(111)_B$ substrate by Plasma Enhanced Chemical Vapor Deposition. It is then patterned with nanoscale openings using electron beam lithography, reactive ion etching and a final HF dip just before the introduction of the wafer under-ultra high-vacuum for growth. The designed patterns include: 1) large area openings of 5µm x 150µm; 2) arrays of parallel trenches oriented in different in-plane directions with nominal widths varing from 50nm to 1µm and lengths from a few µm up to 100µm; 3) crosses, circular and hexagonal rings, with inner and outer diameters of 0.45 and 1.5µm respectively, and 100nm wide circular rings with inner diameter of 1µm. The deoxidization process and growth conditions of samples A, B, C and D are used for the selective area epitaxy of 10nm thick InSb nanostructures on masked $InP(111)_B$ substrates (samples I, J, K and L). Another SAG sample (sample M) is grown with the same conditions as sample G (nominal thickness of 30nm).

The surface morphology of the samples is analysed by means of Scanning Electron Microscopy (SEM) and Atomic Force Microscopy (AFM) in the tapping mode. X-ray diffraction (XRD) using a Panalytical X'pert system is used to probe the relaxation of InSb thin films. To determine the band offsets between InP and InSb, thanks to the UHV connection between the III-V MBE chamber and the XPS/UPS system, we use a commonly employed technique based on a three step analysis [16-18]. Its principle is described in figure 1 in the case of the InSb/InP system. First, the deoxidized InP surface is characterized to measure the binding energy difference between the top of the InP valence band and the P *2p* core level (step 1). Then, an InSb layer with a nominal thickness of 2nm is deposited on the sample using the growth conditions of samples F-H. The quasi-2D growth mode and the thinness of the InSb layer allows to probe the core binding energies in InP and in InSb at the same time. We thus deduce the energy separation between the P *2p* core level in InP and the Sb *4d* core levels in InSb. Finally, a third XPS/UPS analysis is performed after the completion of the growth to a 100nm nominal thickness using the same growth conditions than before. This enables the determination of the binding energy of the Sb 4d core level in bulk InSb. The valence band offset between InSb and InP can then be determined from these different offsets as described in Fig. 1a. The knowledge of the InSb and InP band gaps gives eventually access to the conduction band offset in the heterostructure. For this experiment, a sulphur doped InP (111) substrate with a nominal n-type doping of about $5x10^{18}cm^{-3}$ is used.

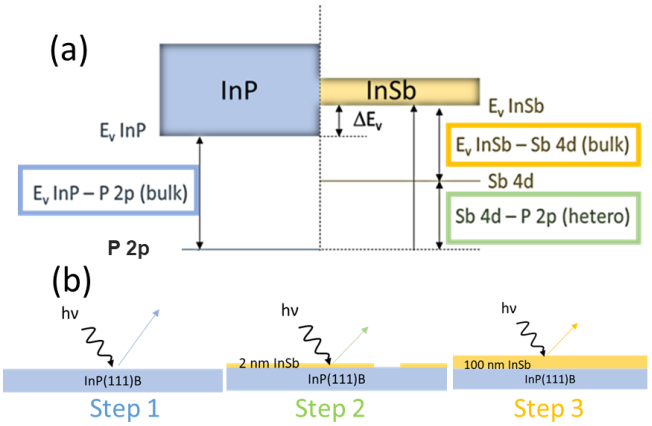

FIG. 1. (a) Band energy diagram for the InSb/InP heterostructure based on the concept of the core level method. The valence band offset is determined from the energetic separation of the bulk components of the P 2p and Sb 4d measured on each side of the interface relative to the difference in the binding energies of the core levels in the pure layers. (b) Principle of the core level method measured with photoelectron spectroscopy.

The electrical properties of InSb thin films grown on semi-insulating InP:Fe (111) are determined using Hall measurements after the fabrication of millimeter scale Van der Pauw devices by means of optical lithography and mesa chemical etching.

The InSb nanostructures grown by SAG are characterized by SEM and Transmission Electron Microscopy (TEM) after Focus Ion Beam (FIB) preparation of thin lamella. Eventually, InSb SAG nanostructures are also analyzed by means of scattering-type Scanning Near-field Optical Microscopy (s-SNOM). Infrared images were acquired with neaSNOM and neaSCOPE microscopes (Attocube systems AG), where a metallic AFM tip (Arrow NCPt or Nano-FTIR) is illuminated by a focused laser beam from a quantum cascade laser with wavelengths of 8.86µm or8 µm. The backscattered light from the tip is detected using a pseudo-heterodyne scheme where both the near-field amplitude and phase are recorded

simultaneously with the sample topography [16]. The optical signals are demodulated at the third harmonic of the tip tapping frequency Ω to suppress the background contribution.

III. RESULTS AND DISCUSSION

a. Structural and electronic properties of thin films

The morphology of the 10nm-thick InSb film deposited on InP(001) is displayed in the SEM and AFM images of figure 2 for samples A to E. Clearly, whatever the investigated growth conditions are, the samples exhibit dispersed facetted InSb islands formed by the diffusion of indium adatoms on the InP surface. The size, density and shape of the islands slowly evolve with the growth conditions. At the smallest growth rate of 0.05ML.s^{-1} (Fig. 2a), the sparse islands have a rectangular shape, elongated towards the [110] in-plane direction. Their morphology does not much change at 0.1ML.s^{-1} (Fig.2b), but their density slightly increases. At 0.2ML.s^{-1} (Fig.2c), the density further increases. This effect takes place with a reduction of the island size and a much less-defined rectangular shape. Increasing the antimony flux to 6ML.s^{-1} (with respect to 2ML.s^{-1} for figures 2a to c) results in an increase of the islands elongation as it can be seen in Fig.2d. The same growth rate and Sb flux but a higher growth temperature lead to a reduction of the islands elongation (Fig.2e). This observation is confirmed by extracting their height profiles in each direction and measuring the mean in-plane aspect ratio of the islands. Whereas a ratio of about 2 between the width of the islands in the [110] and the [1-10] directions is measured for the growth occurring at 390°C, a mean ratio of about 1.5 is achieved at 405°C (Fig.2h). Moreover, based on these profiles, the angle that the side facets form with the top (001) facet is between 45° and 60°. We attribute the difference of angles between two opposite facets to a measurement artefact caused by a convolution between the island profile and the AFM tip shape. In case of an apex which is not symmetric, a small tip slope will underestimate the facet angle. Therefore, the measured angles are consistent with rectangular islands delimited by {111} facets forming an angle of 54° with respect to the top (001) surface. In this hypothesis, $\{111\}_A$ facets would end the islands in the [110] direction whereas $\{111\}_B$ facets would end the islands in the [1-10] direction, in a similar manner than what has been observed during the growth of GaSb on GaP(001) [20]. We explain the elongation of the islands at large Sb/In flux ratio by the Sb saturation of the In incorporation sites on the $\{111\}_B$ side facets resulting in an enhanced diffusion of these adatoms to the $\{111\}_A$ facets, as for GaSb islands grown on GaP. At higher temperature (405°C), the island anisotropy is reduced because of the stronger reevaporation of Sb making the saturation effect less effective. These results indicate that the InSb$(111)_B$ surface energy is minimized at large Sb flux for a moderate growth temperature [21]. Therefore, we speculate that the growth of InSb on an InP$(111)_B$ substrate with the same conditions should promote the formation of two dimensional (2D) InSb islands and their further spreading.

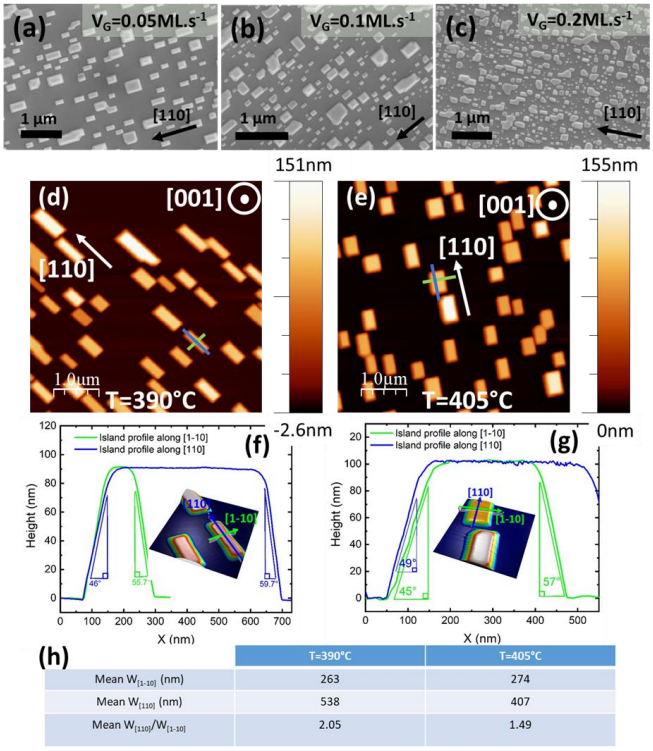

	T=390°C	T=405°C
Mean $W_{[1-10]}$ (nm)	263	274
Mean $W_{[110]}$ (nm)	538	407
Mean $W_{[110]}/W_{[1-10]}$	2.05	1.49

FIG. 2. SEM images of a 10nm-thick InSb layer grown on InP (001) substrate at 390°C with a Sb flux of 2ML/s and a nominal growth rate of 0.05ML.s^{-1} (a), 0.1 ML.s^{-1} (b) and 0.2ML.s^{-1} (c). AFM image of 10nm-thick InSb layer grown on InP(001) substrate with a growth rate of 0.05ML/s and a Sb flux of 6ML/s at 390°C (d) and 405°C (e). The black arrows indicate the orientation of the [110] crystal direction. Scale bar is 1µm. (f) and (g) Height profiles on the InSb islands highlighted in (d) and (e) respectively. They were measured along the [1-10] (green line) and [110] (blue line) directions indicated by green and blue lines in (d). Insets: 3D views of the islands. (h) Table of the mean lateral dimensions of both islands measured in (d) and (e) and mean value of the island aspect ratio.

This is in indeed what is observed when the growth occurs on an InP$(111)_B$ substrate. After a few minutes of growth, two superimposed 2x2 RHEED patterns with different periods can be observed indicating the formation of 2D relaxed InSb islands (Fig. S1 in supplementary information). Progressively, the RHEED pattern with the larger period disappears as the InP surface becomes completely covered with InSb and a streaky 2x2 RHEED pattern characteristic of a Sb-rich InSb$(111)_B$ surface remains. From the AFM image of samples I, J, K and sample F (Fig. 3a-3d), we extracted the InSb coverage of the InP surface with respect to the growth rate and the Sb flux. As shown in Fig. 3e, the surface coverage increases with smaller growth rates, as well as higher Sb/In flux ratio. For the largest Sb flux, a quasi-2D layer with 90% coverage of the InP surface is achieved for a nominal thickness of only 10 nm (inset of figure 3e).

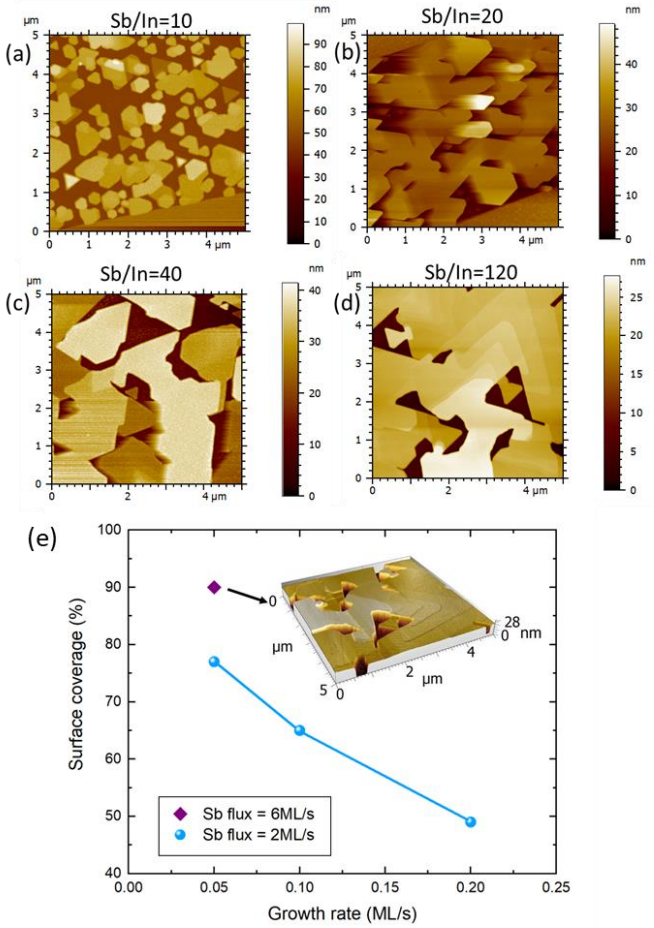

FIG. 3. AFM images of the surface of samples I (a), J (b) and K (c) in large area patterns and un-patterned sample F (d). Evolution of the InSb surface coverage for these different samples with respect to the growth rate and Sb flux (e). The blue circles correspond to a Sb flux of 2ML.s^{-1} and the purple diamond to a Sb flux of 6ML.s^{-1}. The blue line is used as a guidance. Inset: 3D AFM image of sample F.

The SEM micrographs of figure 4 obtained for different deposited thicknesses confirm the preferred 2D growth mode. With increasing thickness, the remaining holes in the InSb layer are progressively filled, causing a reduction of the surface roughness. For a 100 nm-thick layer, only a small density ($2.6x10^5cm^{-2}$) of nanoholes remains, one of which being highlighted in the inset of Fig. 4e. These nanoholes are attributed to the initial formation of twin defects, as suggested by the 180° rotated triangular hillock zoomed in the inset of figure 4a. In the area free of nanoholes, a very smooth surface is obtained with atomically flat terraces. Their length can exceed several hundredths of nanometers (Fig. 4g). These terraces show a 3x3 reconstruction when the surface is deoxidized by atomic hydrogen bombardment at 200°C and subsequently imaged with scanning tunnelling microscopy in UHV [22]. Additional XRD analyses of samples F, G and H (Fig. 4b, 4d and 4f) show that the InSb film is almost fully relaxed since the very beginning of the growth with a relaxation rate of 95% after 10nm and >99% after 30nm. This observation is fully consistent with a direct plastic relaxation by the formation of an interface array of misfit dislocations associated with an island growth mode owing to the very large 14% mismatch between InSb and InP.

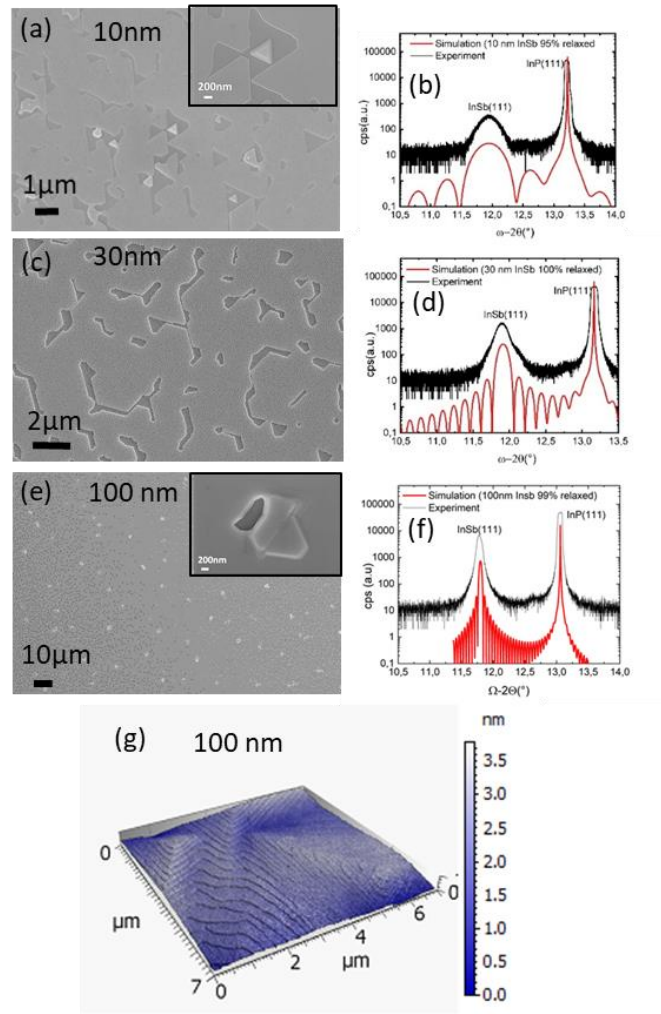

FIG. 4. SEM micrographs (a, c and e) and XRD spectra (b, d and f) of InSb films on InP(111)$_B$ with a nominal deposited thickness of 10nm (sample F), 30nm (sample G) and 100nm (sample H) respectively. Insets of fig 4a and 4g display magnified views of hillocks. AFM image of the surface of sample H measured in an area free of hillocks and nanoholes (g).

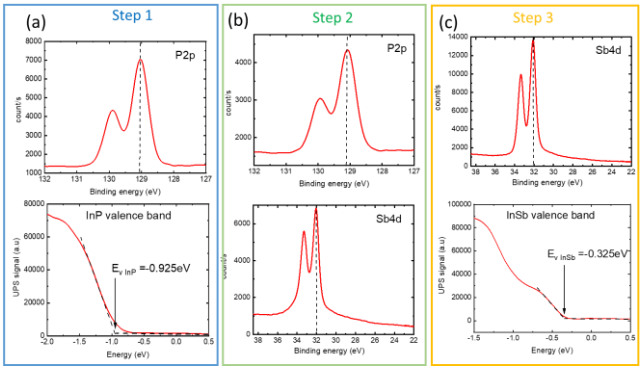

FIG. 5. (a) XPS spectrum of the P2p core level and UPS spectrum of the valence band for the InP (111)$_B$ surface. (step 1 in fig. 1 (b)). (b) XPS spectra of the P2p and Sb 4d core levels after the deposition of a 2nm-thick InSb layer on the InP (111)B surface (step 2 in fig. 1(b)). (c) XPS spectrum of the Sb 4d core level and UPS spectrum of the valence band after the growth of a 100nm-thick InSb layer on the InP (111)$_B$ surface (step 3 in fig. 1(b)).

While the InSb and InP band gaps are well known, the band offsets of InSb/InP heterostructures have been much less investigated and strongly depends on the degree of strain [23]. Based on the core level method described above, the P *2p* core level and the valence band spectra of the deoxidized $InP(111)_B$ surface are first measured with XPS and UPS respectively (figure 5a). The top of the valence band is determined by a linear extrapolation of the valence band spectrum from the high-energy edge to zero intensity. An energy difference of 128.1eV between the P *2p* core level to the top of the valence band is found, which is within experimental uncertainty well consistent with the values reported in the literature for the InP (001) surface (128.2eV in Ref. [24] and 127.8eV in Ref. [25]). Upon the deposition of 2nm of InSb on the InP surface, a core level separation of 97.0eV is measured between the P *2p* and Sb *4d* peaks as seen in Fig. 5b. Finally, the Sb *4d* core level and the valence band spectrum of the 100nm-thick InSb layer grown on $InP(111)_B$ are measured with XPS and UPS respectively (figure 5c). Based on the structural analysis of this overlayer shown in figure 4(g-i), the core level can be considered to have an energy similar to the one of bulk InSb. As to the Fermi level, it lies in the conduction band, in agreement with previous works where the 2x2 reconstruction of the $InSb(111)_A$ surface pins the Fermi level in the conduction band [26], [27]. An energy difference of 31.8eV between the top of the InSb valence band and the Sb *4d* core level is measured. From all these data, the valence band offset between InP and InSb is estimated to be 0.71 ± 0.02eV. It is closed to the theoretical prediction of 0.75eV, which do not include any strain in the layer [28]. Considering an InSb bandgap of 0.17eV at 300K, this implies a conduction band offset between InP and InSb of 0.46eV with a type I configuration. Consequently, close to the InSb/InP interface, the maximum of the valence band of InSb is lying above the mid gap of the InP substrate. As the Fe dopants are known to act as mid gap traps responsible of the semi-insulating properties of InP, they could thus constitute remote acceptors for valence band electrons in InSb, resulting in a remote p-type doping of the InSb layer. At the opposite side of the InSb layer, the UPS spectrum of Fig. 5(c) yields a valence band edge much below the Fermi level, which thus lies in the conduction band. This surface pinning in the InSb conduction band is attributed to the Sb-rich growth conditions as interpreted in Ref. [29]. If this property subsists after air exposure, this means that the surface states act as donors for the oxidized InSb layer.

To further understand the impact of the band alignment on the electrical properties of InSb, Hall measurements on InSb thin films grown on semi-insulating InP (111) with different thickness have been performed. The results, plotted in figure 6a, show a strong evolution of the transport properties with film thickness and temperature. They are attributed to a subtle balance between the contributions of thermally activated bulk intrinsic carriers, electrons provided by surface states and holes provided by remote doping with Fe atoms present in the substrates. At room temperature for the thickest sample, the significant contribution of the thermally activated bulk electrons to the transport properties leads to a quite large mobility of $3980 cm^2.V^{-1}.s^{-1}$ and a n-type Hall density. When the thickness of the InSb layer is reduced to 30nm, the relative contribution of electrons, which we assume to be provided by the surface states, increases with respect to the bulk charges. This results in an increase of the Hall density as the same amount of electrons provided by surface states is concentrated in a reduced volume. Due to the proximity of the InSb surface, the Hall mobility degrades. For the very thin 10nm layer, the large confinement energy of electrons probably leads to an inversion of the role of surface states, which act now as traps instead of donors. The transport properties are then dominated by the holes provided by the remote doping from the substrate, explaining the p-type Hall density and the low Hall mobility. At 77K, the contribution from thermally activated bulk carriers is no longer significant. For the thick sample, the Hall transport properties are governed by electrons provided by surface states. When the thickness of the layer decreases and the confinement energy of electrons becomes larger than the activation energy of surface states, the Hall density turns to p-type as only holes provided by remote substrate doping subsist.

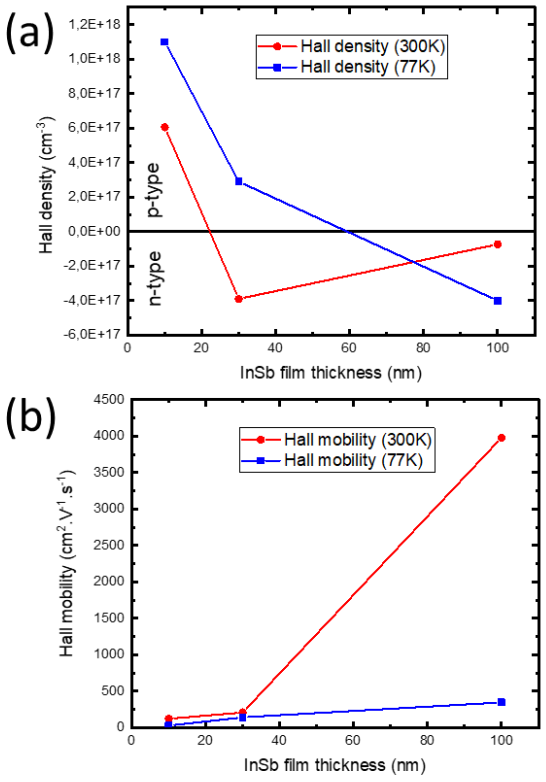

FIG. 6. Hall measurements performed on Van der Pauw devices fabricated from samples F, G and H: evolution of the (a) Hall density and (b) the Hall mobility with respect to the film thickness and temperature.

b. Structural and electronic properties of SAG nanostructures

Figure 7 displays the SEM micrographs of in-plane InSb NW arrays observed on patterned samples I, J, K and L after 10 nm deposition. First, a very good selectively can be noticed thanks to the use of atomic hydrogen flux during the growth. Then, consistently with the surface coverage measured on un-patterned InP surface (Fig. 2), increasing the Sb/In flux ratio leads to an increase of the InSb islands size grown inside the SiO_2 openings. For the narrowest openings (200nm width and below), an almost complete filling of the slits is reached, resulting in 10nm thick in-plane NWs as long as 10µm. Setting

the Sb/In flux ratio at the highest value of 120, a very good yield is achieved after the deposition of 30nm (sample M). Most of the nanoscale openings exhibit a full filling with a homogenous thickness, as confirmed by the SEM images of sample M displayed in figure 8. This figure shows different arrays of NWs, crosses and ring nanostructures. 100µm long in-plane NWs with exceptional length/thickness and length/width aspect ratios of 10000 and 1000 respectively are achieved (Fig. 8e and 8f).

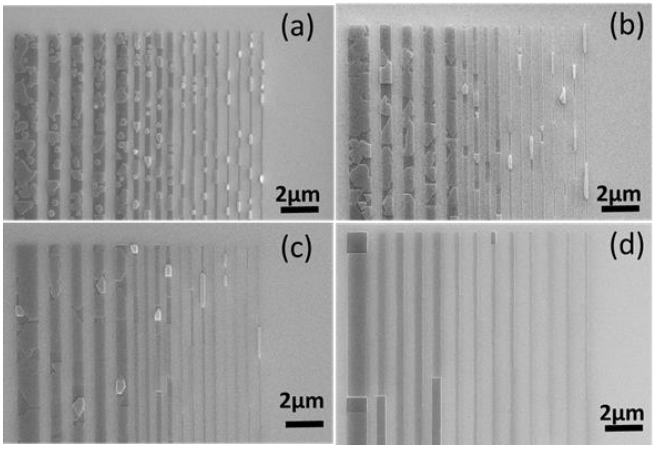

FIG. 7. 10nm InSb deposited by atomic H-assisted MBE into SiO_2 openings forming an array of nanoribbons with different widths from 1µm (first ribbon from left), 500nm (ribbons 2 to 5), 200nm (ribbons 6 to 9), 100nm (ribbons 10 to 13) and 50nm (four last ribbons to the right). The Sb/In flux ratios during the growth are 10 (a), 20 (b), 40 (c) and 120 (d) corresponding to samples I to L.

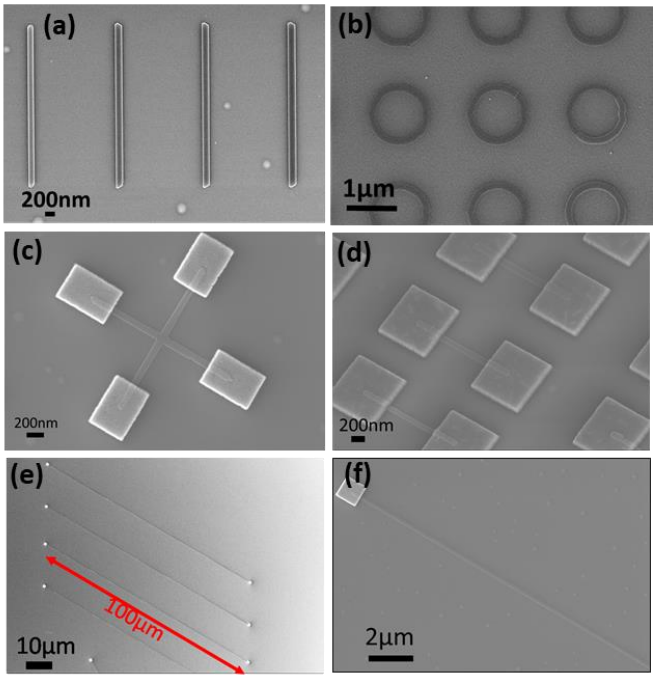

FIG. 8. SEM image of arrays of 30nm thick InSb deposited under optimized growth conditions (sample M) inside 100nm wide straight (a) or ring (b) SiO_2 openings designed on an $InP(111)_B$ substrate. SEM images of 30nm thick InSb in-plane nanostructures after metal contact deposition: 3µm long cross (c), array of 1µm long straight NW (bird view) (d) and array of 100µm long and 100nm wide NWs (e and f).

The TEM investigations carried out on 100nm wide $[\mathbf{01\bar{1}}]$ oriented NWs are summarized in figure 9. The STEM cross-section image (Fig. 9a) confirms the high crystal quality of the grown material as no threading defect can be observed. We can notice the flat top (111)-surface and the flared out shape of the cross-section due to the HF chemical treatment used for the final opening of the SiO_2 mask (Fig. 9f). The energy dispersive X-ray (EDX) mapping of the composition of another $[\mathbf{01\bar{1}}]$ oriented NW (Fig. 9b to 9e) confirms the chemical quality of the nanostructure and the abruptness of the interface with the substrate (the dark gray top part of the nanoribbons is due to an insufficiently thick protection layer during the lamella preparation with FIB, leading to Ga implantation in this area). The structural quality of InSb and of the interface with the substrate is highlighted in Fig. 9g. The Fast Fourrier Transform based numerical treatment of the red square area from Fig. 9g brings out the periodic array of misfit dislocations located at the InSb/InP interface (Fig. 9h). Consistently with the almost full relaxation of the InSb thin films observed in Fig. 3, the average distance of 3.24 nm between the dislocation cores, which is deduced from this figure, coincides with the theoretical distance value *d* for a full plastic relaxation (3.26nm) given by (Eq.1):

$$\boldsymbol{d} = \frac{\boldsymbol{a}_{\boldsymbol{InP(111)}}}{|f|\sqrt{3}} \qquad \text{(Eq.1)}$$

where $\boldsymbol{a}_{\boldsymbol{InP(111)}}$ is the lattice constant of InP and *f* the lattice mismatch between InSb and InP.

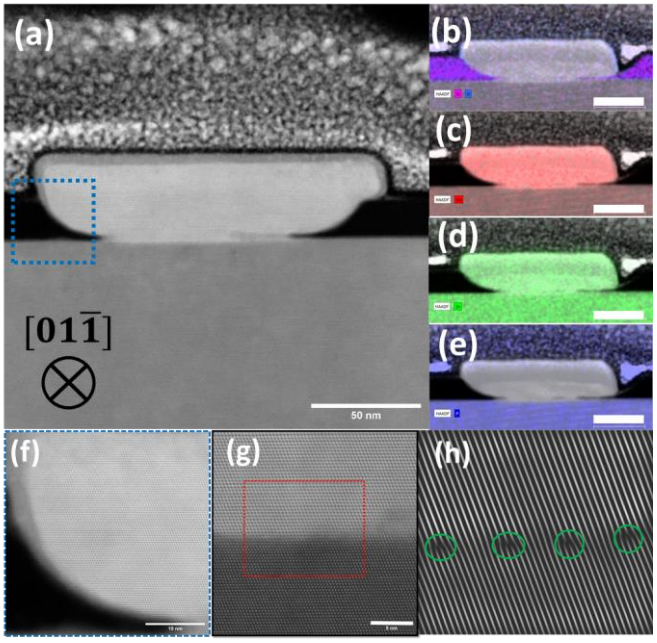

FIG. 9. (a) HAADF-STEM cross section image of a $[01\bar{1}]$ InSb NW grown by SAG on InP(111)B under large Sb flux (a). Scale bar is 50nm. EDX elemental mapping of the cross-section of a NW highlighting (b) Si (pink) and O (light blue), (c) Sb (red), (d) In (green) and (e) P (blue). Scale bar is 40 nm. (f) Magnified view of the area delimited by a blue dashed square in (a). Scale bar is 10 nm. (g) High resolution image of the InSb/InP interface. Scale bar is 5 nm. (h) Numerical filtered image of the red dashed square area in (g) highlighting the interface misfit dislocations (green circles).

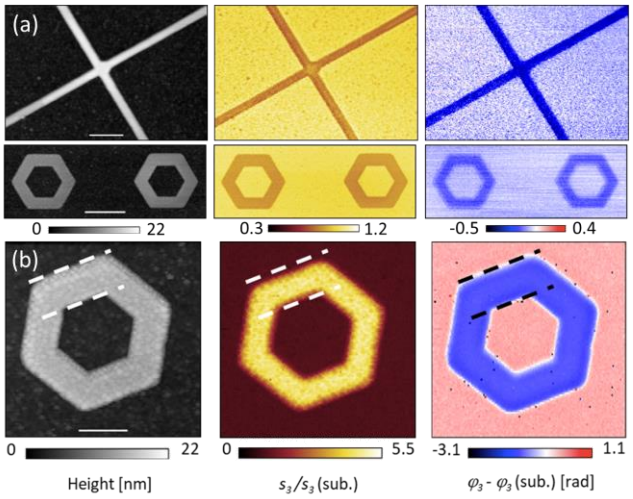

FIG. 10. Topography (first column), third harmonic amplitude s_3 (second column) and phase φ_3 (third column) of the s-SNOM signal measured on 30nm thick InSb nanostructures (sample M) for different excitation wavelengths. (a) Images for a wavelength of 8.86µm. First line: 100nm wide cross. Second line: 200 nm wide hexagonal rings. Scale bars are 500nm (top) and 1µm (bottom). (b) Image of a 200nm wide ring (rotated by 30° with respect to the previous ones) with a wavelength of 8µm. Scale bar is 500nm. Parallel dashed lines are used to compare the width of the ring on the different maps. For each image, third harmonic amplitudes and phases have been normalized to the s-SNOM signal of the SiO_2/InP substrate following the procedure of ref [30].

Finally, we investigated the structure and optical properties of the in-plane SAG nanostructures of sample M using s-SNOM in the mid-infrared range. As shown in Fig. 10, the quite homogeneous contrast in the s_3 and φ_3 signals, suggests the absence of crystal defects in the volume of the nanostructures, in agreement with the TEM analysis. Small fluctuations in the s_3 signal are related to the surface roughness of InSb due to some surface oxidization over time. It has been demonstrated that the near-field optical response of semiconductors depends on the doping concentration n, with a resonance behaviour that arises from the near-field interaction between the tip and the free carriers (plasmons), which can be described by a Drude model [30-32]. However, for the relatively low doped InSb ($n \approx 4.10^{17}cm^{-3}$ assumed for sample M), previous experiments have shown no clear plasmon resonance, with a near-field response similar to that of silicon in the 800 – 1000cm^{-1} range [32]. In addition, the calculated near-field spectra of the semi-insulating InP substrate are frequency-independent and close to that of gold [30]. Therefore, we acquired images in the region of the SiO_2 optical phonons (Fig. 10), and the improved optical contrast is mainly due to a difference in the dielectric function between the InSb nanostructures and the SiO_2/InP substrate. For a 10nm thick SiO_2 layer, a maximum in s_3 is expected at around λ= 8.86µm (ω = 1129cm^{-1}), whereas there is a maximum of absorption (related to φ_3) close to λ = 8µm (ω = 1250cm^{-1}) [33, 34]. This is evidenced by a contrast inversion in both s_3 and φ_3 images acquired at λ=8.86µm (fig. 10a) and λ=8µm (fig. 10b). In all images the phase signal was corrected to account for a linear vertical phase drift. Both optical amplitude (s_3) and phase (φ_3) images are normalized to the SiO_2/InP substrate. Comparing topography, amplitude and phase mapping of the s-SNOM signal of the hexagonal ring at 8µm wavelength (Fig. 10b), we can notice a difference between the width of the ring in the three images. As revealed by the dashed lines, the narrower width of the ring in the amplitude map with respect to topography and phase ones (320nm instead of 360nm) is attributed to the lateral growth of InSb over the mask consistently with the cross-sectional TEM analyses of the nanowires. Interestingly, even though there is an edge-darkening effect, resulting in a lower amplitude signal across the edges [33], the extension over the mask seems larger in the outer part of the ring than in the inner part suggesting a larger collection of adatoms from the outer facets of the InSb ring than the inner ones. Such a phenomenon could indicate a sink growth mode [35] and a diffusion length of In on the mask larger than the inner radius of the ring. s-SNOM thus appears as a powerful non-destructive method to investigate the lateral overgrowth of nanostructures.

IV. CONCLUSION

In summary, after optimising the 2D nucleation of InSb on $InP(111)_B$ substrates by using a very large Sb/In flux ratio during the growth, we have demonstrated the growth of high quality in-plane InSb nanostructures by atomic hydrogen-assisted selective area MBE. The variety of dimensions and shapes that can be designed as well as the precise positioning of the nanostructures are very attractive to build complex quantum devices such as Aharonov-Bohm oscillators evidencing quantum interferences or crossing nanowires arrays for Majorona Zero Mode braiding experiments. However, the Hall measurements performed on 2D layers highlights the strong impact of surface states on the transport properties in the material and the importance to develop an efficient passivation of the surface for the fabrication of future devices.

Data availability statement

All data that support the findings of this study are included within the article (and any supplementary files).

ACKNOWLEDGEMENTS

This study was financially supported by the French National Research agency under the program Equipex EXCELSIOR and (projects INSPIRING ANR-21-CE09-0026-01, COMI ANR-17-CE24-0002 and HYPSTER ANR-20-CE42-0016), the French Technological Network Renatech, and the Région Hauts de France.

REFERENCES

[1] Dvir *et al.*, Nature 614, 445–450 (2023). https://doi.org/10.1038/s41586-022-05585-1
[2] Kuo *et al.*, Nanoscale Res Lett 8, 327 (2013). https://doi.org/10.1186/1556-276X-8-327
[3] Zijin Lei et al 2024 J. Phys.: Condens. Matter 36 383001 https://doi.org/10.1088/1361-648X/ad5246
[4] Orr *et al.*, Phys. Rev. B77, 165334 (2008) https://doi.org/10.1103/PhysRevB.77.165334
[5] Williams *et al.*, J. Appl. Phys 63, 1526 (1988) https://doi.org/10.1063/1.339936

[6] Greene *et al.*, Semicond. Sci. Technol. 5, S311 (1990) https://doi.org/10.1088/0268-1242/5/3S/070
[7] Thainoi et al, Journal of Crystal Growth, 621, 127366 (2023) https://doi.org/10.1016/j.jcrysgro.2023.127366
[8] Caroff *et al.*, Small 2008, 4 , 878 https://doi.org/10.1002/smll.200700892
[9] Plissard *et al.*, Nano Lett. 2012, 12, 1794 https://doi.org/10.1021/nl203846g
[10] Yang *et al.*, Crystal Growth Design 2010, 10, 2479 https://doi.org/10.1021/cg100376u
[11] Thelander et al., Appl. Phys. Lett. 100 (23), 232105 (2012) https://doi.org/10.1063/1.4726037
[12] Rossi et al, Nanotechnology, 35(41), 415602 (2024) https://doi.org/10.1088/1361-6528/ad61ef
[13] Desplanque *et al.*, 2018 Nanotechnology 29 305705 https://doi.org/10.1088/1361-6528/aac321
[14] Op het Veld *et al*, Commun Phys 3, 59 (2020). https://doi.org/10.1038/s42005-020-0324-4
[15] Aseev *et al*, Nano Lett. 19, 9102-9111 (2019) https://doi.org/10.1021/acs.nanolett.9b04265
[16] Waldrop *et al*, J. Vac. Sci. Technol. 11 1617–20 (1993) https://doi.org/10.1116/1.586491
[17] Dehaese *et al*, J. Appl. Phys. 84, 2127–2132 (1998) https://doi.org/10.1063/1.368357
[18] Desplanque *et al*, J. Appl. Phys. 108, 043704 (2010) https://doi.org/10.1063/1.3475709
[19] N. Ocelic et al., Appl. Phys. Lett., (200) https://doi:10.1063/1.2348781
[20] El Kazzi *et al*, J. Appl. Phys. 111, 123506 (2012) https://doi.org/10.1063/1.4729548
[21] He et al, Applied Physics Letters, 125, 223104 (2024) https://doi.org/10.1063/5.0223513
[22] W Khelifi *et al*, Rev Sci Instrum 2023 1, 94, 123702 https://dx.doi.org/10.1088/1361-6528/acc810
[23] Utzmeier *et al*., Phys. Rev. B 56, 3621 (1997) https://doi.org/10.1103/PhysRevB.56.3621
[24] Waldrop *et al*, Appl.Phys.Lett. 54, 1878 (1989) https://doi.org/10.1063/1.101246
[25] Biadala *et al*, ACS Nano 13, 1961 (2019) https://doi.org/10.1021/acsnano.8b08413
[26] Hernadez-Calderon *et al*, Surface Science 152/153, 1035 (1985) https://doi.org/10.1016/0039-6028(85)90518-7
[27] Olsson *et al*, Phys. Rev. B 50, 18172 (1994) https://doi.org/10.1103/PhysRevB.50.18172
[28] J.Tersoff, in Heterojunction Band discontinuities, edited by F. Capasso and G. Margaritondo, North-Holland, Amsterdam, 1987
[29] Dong et al, J. Vac. Sci. Technol. B 41, 032808 (2023) https://doi.org/10.1116/6.0002606
[30] Stiegler et al. Nano Lett. 10, 4, 1387 (2010) https://doi.org/10.1021/nl100145d
[31] Huber et al., Nano Lett. 8, 11, 3766 (2008) https://doi.org/10.1021/nl802086x
[32] Xue et al., Adv. Mater. 35, 14, 2208952 (2023) https://doi.org/10.1002/adma.202208952
[33] Chen et al., Optics Exp. 29, 24, 39648 (2021) https://doi.org/10.1364/OE.440821
[34] Zhang et al., Phys. Rev. B, 85, 7, 075419 (2012) https://doi.org/10.1103/PhysRevB.85.075419
[35] Cachaza et al. Phys. Rev. Mat. 5, 094601 (2021) https://doi.org/10.1103/PhysRevMaterials.5.094601